Early Detection of Tau Pathology

Parag Parekh[1], Andrew Badachhape[1], Qingshan Mu[1], Rohan Bhavane[2], Mayank Srivastava[2], Igor Stupin[2], Prajwal Bhandari[1], Laxman Devkota[1], Jason Eriksen[3], Eric Tanifum[4], Ketan Ghaghada[4], and Ananth Annapragada[4,*]

[1]Baylor College of Medicine, Houston, TX, USA, [2]Texas Children's Hospital, Houston, TX, USA, [3] College of Pharmacy, University of Houston, Houston, TX, USA, [4]Texas Children's Hospital/Baylor College of Medicine, Houston, TX, USA

Email: annaprag@bcm.edu/avannapr@texaschildrens.org

Abstract

While a definitive Alzheimer's disease (AD) diagnosis remains a post-mortem exercise, the ATN Research Framework proposed by the National Institute on Aging and the Alzheimer's Association utilizes a score representing the presence of amyloid deposits (A), tau deposits (T) and neuronal degeneration markers (N), with A+T+ necessary for a positive diagnosis. Current detection of tau pathology lags amyloid detection by years and by the time both markers are detected the disease is fairly advanced. We describe the development of a new generation of molecular imaging probes for *in vivo* detection of cells undergoing abnormal phosphorylation representing the initial stages of pTau pathology, potentially enabling a very early stage diagnosis of AD. We describe a novel nanoparticle formulation that binds such abnormally phosphorylating cells in a mouse model of tau pathology, enabling in *vivo* visualization of the hyperphosphorylative state by magnetic resonance imaging. Our results demonstrate the potential of this novel platform to identify a correlative marker signifying the development of future tau pathology, and has implications for early-stage diagnosis of Alzheimer's disease.

Introduction

The microtubule associated protein tau, coded for by the *MAPT* gene, is abundant in the brain and is present in neurons, glia and other cell types. Tau shows immense diversity. It is expressed in six isoforms and has a vast array of post-translational modifications, including glycosylation, glycation, nitration, ubiquitination and more than 80 phosphorylation sites expanding the complexity of its role in health and disease[1,2]. A definitive feature of many neurodegenerative diseases including AD, frontotemporal lobar degeneration (FTLD), Parkinson's disease (PD) is the presence of intracellular aggregated filamentous tau (collectively termed

30 “tauopathies”)[3–6]. This pathogenic insoluble tau been implicated in disease progression in these dysfunctional
31 brains. The transition from physiological soluble tau is primarily associated with changes in its phosphorylation
32 state leading to oligomeric tau[7], then tau fibrils known as paired helical fragments (PHF) that collectively form
33 characteristic neurofibrillary tangles (NFT). The tau aggregates are then capable of “infecting” a healthy cell
34 inducing further misfolding, aggregation, and neuro-toxicity[8,9]. Studies of intercellular propagation demonstrate
35 passage through an extracellular phase that progresses throughout the brain [10,11].

36 The research framework proposed for precise diagnosis of AD by the National Institute of Aging-
37 Alzheimer’s Association (NIA-AA) categorizes extracellular deposits of amyloid beta (A), presence of
38 intraneuronal hyperphosphorylated tau (T) and markers of neurodegeneration or neuronal injury (N). Each
39 biomarker is scored either positive or negative[12]. To be on the AD continuum, A+ (Amyloid positive) is required,
40 while a positive diagnosis of AD requires A+ and T+. Biomarker detection can be by i) positron emission
41 tomography (PET) imaging of amyloid and tau or, ii) cerebrospinal fluid (CSF) detection of reduced $A\beta_{42}$, and/or
42 high $A\beta_{40}$/ $A\beta_{42}$ and high phosphorylated tau and total tau, or iii) neuronal injury or degeneration as shown by
43 structural brain magnetic resonance imaging (MRI)[13]. Tracking of brain pathology in longitudinal studies suggests
44 that tau pathology may precede the accumulation of Aβ, but is undetectable as it is below current biomarker
45 detection threshold levels, and is amplified catastrophically by independent Aβ deposition [14–16]. ATN research
46 framework based diagnosis of AD is therefore limited by tau pathology detection, providing an impetus to develop
47 specific and sensitive tau detection methods for earlier diagnosis.

48 Other factors to consider in the development of tau detection methods include the invasive nature of
49 CSF sampling requiring lumbar puncture, and in the case of PET imaging, exposure to ionizing radiation, high
50 cost, well documented side effects, irregular availability in primary care setting, and uneven geographical
51 availability of PET scanners and isotopes[17–21]. The short half-life of PET agents also poses challenges for the
52 detection of intracellular tau in the early stages of tau pathology formation[22]. Blood based markers are very
53 promising, but only provide an indirect measure that cannot provide information on the localization of tau
54 pathology in brain[23–26]. Methods to detect early tau pathology that avoid these pitfalls are therefore highly
55 desirable.

56 The initiation of tau pathology is marked by abnormal phosphorylation of tau[27,28]. We hypothesize that
57 hyperphosphorylative conditions in neurons, consistent with an altered balance of kinase-phosphatase activity
58 resulting in elevated levels of hyperphosphorylated tau species, result in unique surface markers[29–31]. We

59 envisioned a targeted contrast-enhanced MRI test identifying the earliest stages of tau pathology represented by
60 cells in the process of abnormally phosphorylating tau. We used an iterative Cell-SELEX process to identify DNA
61 thioaptamers that specifically bound such cells[32,33]. The use of phosphorothioate modified aptamers enhances
62 stability under physiological conditions. High T1 relaxivity PEGylated liposomes bearing macrocyclic Gd-
63 chelates[34] were modified to bear the aptamers on their surface, thus enabling targeting of the particles to the
64 surface of hyperphosphorylative cells for contrast-enhanced MRI. At the molecular level, we sought the binding
65 targets of the aptamers, identifying vimentin, a normally intracellular protein that interestingly is specifically
66 expressed on the surface of cells under hyperphosphorylative conditions, and representing a possible biomarker
67 of pathological hyperphosphorylation found in AD.

68 **Results**

69 **Validation of cell surface changes in hyperphosphorylative conditions**

70 SH-SY5Y, a human neuroblastoma cell line that can be differentiated into neuron-like cells by changes
71 in culture medium was used to model cell-surface changes under hyperphosphorylative conditions (Fig 1B). We
72 used retinoic acid (RA) to induce cell differentiation marked by temporal changes in morphology including the
73 formation and lengthening of neurites and with a strong increase in levels of intracellular tau. Imbalance in the
74 kinase and phosphatase activity leading to hyperphosphorylation, simulating early stages of tauopathies, was
75 induced by the use of a cell permeable neurotoxin okadaic acid (30nM, 24 h) (OA)[35], and confirmed by the
76 increase in phosphorylated tau S396 (Supp. Fig. 1). In parallel experiments, a milder agent, excitotoxin quinolinic
77 acid (QA) 1μM for 24 h was also used to induce hyperphosphosphorylation[36].

78 A reverse phase protein array (RPPA) assay was conducted to test the hypothesis that
79 hyperphosphorylation results in compositional changes reflected on the cell-surface. RPPA analysis
80 demonstrated marked cell surface changes in hyperphosphorylative cells including over-expression of cell
81 surface receptors. RPPA assessment with a panel of 221 proteins across different pathways and post-
82 translational modifications including phosphorylation examined SH SY5Y cell lysates under differentiated and
83 hyperphosphorylative states. We identified 98 proteins and 36 phosphorylated proteins that showed significant
84 change in their expression under different conditions (**Fig 1C**). Uniprot [37] protein associations showed 44 cell-
85 membrane associated proteins, 10 peripheral membrane or 12 single-pass membrane proteins were significantly
86 altered under hyperphosphorylative conditions.

87 ## Screening for aptamers that bind cells in hyperphosphorylative state

88 Aptamer screening was performed using the cell-SELEX approach on differentiated SH-SY5Y cells in a
89 hyperphosphorylative state (Fig. 2A). A total of 26 cell SELEX cycles were performed. To remove
90 oligonucleotides that bound common cell surface molecules not specific to the hyperphosphorylative state, a
91 negative selection was introduced at cycles 12 and 13 using differentiated, non hyperphosphorylative cells (i.e.
92 without OA treatment). Anticipating that selected aptamers would be systemically delivered as nanoparticle
93 imaging agents, and the primary toxicity driven by anomalous hepatocyte uptake, we conducted another round
94 of negative selection at cycles 20 and 21 using a hepatocyte cell-line THLE-3 to remove oligonucleotides that
95 exhibited enhanced uptake by hepatocytes.

96 ## Tau1 and Tau3 aptamers specifically bind hyperphosphorylative cells

97 Sequencing of all the selected pools was performed using the Ion Torrent sequencing platform[38] and
98 revealed the evolution of families of DNA sequences, with enrichment particularly evident after 10 rounds of
99 SELEX. Negative selection eliminated certain sequences that were not specific to the hyperphosphorylative state,
100 or promoting hepatocyte uptake. However, the relative abundance of key sequences increased steadily
101 throughout the whole process. The 23 most abundant sequences at round 26 were identified and their abundance
102 throughout the SELEX process as calculated using AptaAligner[39] is shown in Fig. 2B . The sequence Tau1
103 exemplifies this behavior representing a whole 59% of cycle 26. A single base difference from this sequence,
104 Tau3, is the second most represented sequence. The sequences present at the final round were grouped by
105 hierarchical clustering and sequence homology using the multiple sequence alignment code MAFFT [40] showing
106 five distinct families (Fig 2E) also presented as a cladogram (using the Clustal Omega[41]) showing the common
107 ancestry between these five aptamers families (Fig. 2F). Elevated levels of Tau1 binding to the membrane of
108 hyperphosphorylative cells is demonstrated in Figure 2C. The secondary structure of the aptamers Tau1 and
109 Tau3 calculated using mfold[42] is shown in Fig 2D. The apparent equilibrium dissociation constants (Kd_{app}) were
110 measured by serial dilution of aptamer solutions with target hyperphosphorylated and non-target differentiated
111 and undifferentiated SH-SY5Y cells. The affinity of these aptamers was also tested with another immortal neural
112 progenitor stem cell line ReN-VM[43] in hyperphosphorylative and non-hyperphosphorylative conditions . The Kd_{app}
113 for Tau1 and Tau3 with hyperphosphorylated SH SY5Y cells is 0.167 ± 0.015 nM and 0.194 ± 0.032 nM; and
114 for the ReN-VM cells 318.15 ± 46.2 nM and 234.24 ± 38.6 nM respectively (Supp. Fig 2).

115 ## TauX nanoparticles for magnetic resonance imaging

116 For *in vivo* imaging of the hyperphosphorylative state in the brain of live mice, aptamer-targeted
117 nanoparticles were fabricated for use as a molecular MRI contrast agent (TauX). TauX, was formulated as two
118 versions, one using the Tau1 aptamer (TauT1) and another using the Tau3 aptamer (TauT3). Liposomal
119 nanoparticles were synthesized using a lipid mixture that included lipidized Gd-DOTA for MR imaging, cholesterol
120 for liposomal stability; additionally we also incorporated lipidized rhodamine for studying *ex-vivo* microscopic
121 distribution of liposomal nanoparticles in brain tissues using fluorescence microscopy[44,45]. The TauX
122 compositions also included DSPE-mPEG2000 to increase the *in vivo* circulation time[34]. Particles had a
123 hydrodynamic diameter of ~150nm, ~86,000 Gd-chelates per liposomes and ~500 aptamers conjugated to the
124 outer leaflet of each liposomal nanoparticle (Fig.3)

125 ## *In vivo* molecular MRI using TauX for detection of hyperphosphorylative cells

126 To test if TauX could detect the hyperphosphorylative state *in vivo*, MRI studies were performed in a
127 P301S transgenic mouse model of AD-related tauopathy. Studies were performed in transgenic and age-
128 matched wild type mice at 2-3 months of age. At this young age, transgenic animals do not show frank tau
129 pathology (i.e., neurofibrillary tangles), but practically all will develop tau pathology by around 8 months of age.
130 Animals underwent baseline, pre-contrast MRI. Thereafter, animals were intravenously administered MRI
131 contrast agent (TauT1, TauT3 or non-targeted control stealth liposomes that were not expected to provide signal
132 enhancement as they did not have a targeting aptamer). Delayed post-contrast MRI was performed 4 days later.
133 MR images were acquired using a T1-weighted spin-echo (T1w-SE) sequence and a T1-weighted fast spin echo
134 inversion recovery (FSE-IR) sequence[46]. Transgenic mice administered TauT1 and TauT3 demonstrated signal
135 enhancement in the cortex and the hippocampus regions of the brain (**Fig. 4B**). Wild-type mice (WT) administered
136 TauT1 or TauT3 did not show signal enhancement in the brain. Similarly, transgenic mice administered non-
137 targeted liposomal-Gd contrast agent did not show signal enhancement in cortex or hippocampus. These regions
138 of interest were further analyzed quantitatively and signal-enhancement between the transgenic and wild-type
139 mice were found to be statistically significant ($p < 0.05$) (Fig 4D). A baseline enhancement threshold of ~6% (=2X
140 standard deviation of signal in baseline scans) was used as the classification threshold. Animals that showed
141 signal enhancement above the threshold were identified as positives. Receiver operator characteristic (ROC)
142 curves were generated with a six-point ordinal scale to assess sensitivity and specificity for detecting the

genotype, using TauT1 and TauT3 contrast agents, and constructed over the entire tested group, including controls. The aptamer-targeted nanoparticle contrast agents, TauT1 and TauT3, showed overall AUC and accuracy of ~0.95. TauT3 demonstrated higher sensitivity than TauT1.

Post-mortem brain analysis was performed in 2-3 month old transgenic and wild-type mice. Immunofluorescence analysis using AT8 antibody staining revealed the presence of hyperphosphorylated tau species in transgenic mice but absent in wild type mice (**Fig. 4F**). A 100% concordance was observed between AT8 positivity and animal genotype. In summary, *in vivo* studies demonstrated that TauX enabled *in vivo* molecular MRI of the hyperphosphorylative state months before frank tau pathology i.e. the presence of neurofibrillary tangles, becomes evident in transgenic mice.

Target identification of aptamers

To characterize the binding target of the aptamers, we performed an aptamer-based pulldown assay, aptamer-based immunoprecipitation, followed by mass-spectrometry. We performed the assay for both Tau1 and Tau3, aptamers. A ranking of the abundance scores for identified proteins revealed keratin 6a, Keratin 6b and Vimentin as possible binding targets (Table 1). The surface expression of Keratin 6a, 6b was similar on wild-type and transgenic tissue sections whereas the Vim expression was higher in the transgenic mice (Fig 5C). SH-SY5Y cells under undifferentiated, and differentiated hyperphosphorylative conditions show increasing levels of vimentin (Fig.5B) further suggesting it is a potential target of aptamers Tau1 and Tau3.

Discussion

The ATN research framework suggests biomarkers to diagnose and classify AD. Under this framework CSF based detection of Aβ, tau (total, and phosphorylated) have been reported but only at the prodromal stage of disease, in patients with mild cognitive impairment[47]. Non-invasive neuroimaging tools, such as structural MRI to diagnose and monitor neurodegeneration[48] show a definitive correlation with cognitive decline, visualizing atrophic regions that depict neuronal injury in late stage disease[49]. However, a reliable marker of early presymptomatic stage disease is yet to be identified.

While the role of Aβ and tau in the development of AD and the mechanism of transition from presymptomatic to symptomatic AD are yet unclear, the time scale of the transition is generally accepted to be over a period of 10-20 years[14]. Aβ deposits are considered the start of neurodegeneration but recent studies

170 indicate that tau pathology[50] shows a stronger correlation with disease progression suggesting that the limitation
171 of current tests is their inability to identify early stage pathological tau[15]. CSF presence of hyperphosphorylated
172 tau species p-181 and p-217 is associated with Aβ deposition that precedes a positive tau PET[51] but only has a
173 concordance of 50%-70% [52]. Taken as a whole, the roles of Aβ and tau deposition in disease progression and
174 the role of Aβ in the spread of initial tau aggregates, strongly suggest that a biomarker of pathological tau at a
175 presymptomatic stage of the disease is likely to advance detection by several years, and constitutes the
176 motivation for this work.

177 Initial tau aggregation is thought to be triggered by an imbalance in cellular homeostasis caused by
178 dysregulated phosphorylation[53,54]. Several kinases can phosphorylate tau at multiple locations; at least 45 sites
179 have been observed experimentally[55–57]. Combined with reduced phosphatase activities in AD, the altered
180 kinase-phosphatase balance yields hyperphosphorylative conditions that cause abnormal hyperphosphorylation
181 of tau[58]. Disruption of the normal function of tau, modulating microtubule dynamics by lowering its binding
182 capabilities[59] increases the level of cytosolic free tau leading to aggregation and fibrillization of tau that spreads
183 throughout the connected brain, seeding the pathology[60,61]. We hypothesized that this initial process of
184 hyperphosphorylation is associated with changes on the surface of hyperphosphorylative cells. We therefore
185 sought to identify these surrogate markers of tau hyperphosphorylation that presage future tau pathology.

186 Using SH-SY5Y cells as a model of neuronal hyperphosphorylation, we used a reverse-phase protein
187 array (RPPA) analysis to demonstrate elevated levels of surface molecules specific to the hyperphosphorylative
188 state (Fig 1C). Cell-SELEX capturing the differences between the surface of hyperphosphorylative cells and
189 normal cells allowed the selection of phosphorothioate modified short DNA aptamers that bound with high affinity
190 and specificity to hyperphosphorylative cells Fig 2 A. Having identified unique aptamers that bound such markers,
191 we developed MR molecular imaging contrast agents that recognize the surface of cells in hyperphosphorylative
192 state. We acknowledge that SH-SY5Y cells are not true neurons, they are a cell line originating in a
193 neuroblastoma, a tumor of embryological neural crest origin. However, they can be induced to differentiate to a
194 neuronal phenotype (as in the current work). While primary neuronal culture, or immortalized neuronal cells e.g.
195 ReN-VM may offer alternative models of neurons, we have functionally tested the aptamer hits from our SELEX
196 screen in a transgenic mouse model of tau deposition, and validated their performance, supporting our position
197 that the choice of cell model was adequate to identify suitable markers of tau hyperphosphorylation.

198 PET is the leading modality for clinical molecular imaging, driven by its high contrast sensitivity, however,
199 it suffers from poor spatial resolution on the order of 5-10mm, high cost; limited access to radioactive tracers,
200 and radiation exposure. Nanoparticle-enhanced MR imaging overcomes all these obstacles, but historically has
201 not achieved high enough sensitivity. We have previously demonstrated liposomal nanoparticles exhibiting large
202 numbers of Gd chelates in the external bilayer leaflet, with hyper-T1 relaxive properties resulting in contrast
203 sensitivity that rival nuclear imaging[45,62].

204 In P301S mice, the earliest reported histopathological studies are at age of 2.5months[63,64], and report
205 no tau pathology. “Tau seeding” the cell-cell transfer of pathogenic tau aggregates has been reported using brain
206 homogenates at 1.5 month of age[65]. We therefore chose P301S mice at 2 months of age for our studies when,
207 tau seeding should be taking place, but frank tau pathology should be absent. The mice were injected with TauX
208 nanoparticles targeted either by the Tau1 aptamer or the Tau3 aptamer. When imaged by T1-weighted MRI
209 sequences, designed to optimize signal from the Gd chelate induced T1 relaxation caused by the liposomal-Gd
210 nanoparticles, signal enhancement was observed in the cortex and hippocampus regions of the brain.
211 Hyperphosphorylative conditions were confirmed by post-mortem IF staining with AT8 antibody that recognizes
212 the S202 and T305 pTau species. Signal enhancement was not observed in non-transgenic mice, or in transgenic
213 mice injected with untargeted nanoparticles, supporting the specificity of Tau1-or Tau3-bearing nanoparticle
214 binding to target.

215 We have narrowed down the possible binding targets of the aptamers, and our data suggest that cell
216 surface vimentin is a likely target. We have confirmed the specific presence of cell surface vimentin on the surface
217 of SH-SY5Y cells in a hyperphosphorylative state, and on P301S mouse brain sections. Vimentin is an
218 intermediate filament protein that undergoes constant assembly and/or remodeling and is usually associated with
219 mesenchymal cells[66]. The assembly state of filaments is linked to their phosphorylation state, phosphorylation
220 promotes disassembly[67]. Vimentin contains more than 35 phosphorylation sites targeted by multiple kinases and
221 phosphatases allowing it to adjust IF dynamics dependent on its environment[68,69]. Mechanical, chemical (toxins,
222 hypoxia), and microbial stresses upregulate vimentin and its phosphorylation that allows cells to adjust their
223 mechanical properties[70,71]. The balance of different oligomeric forms influence dynamic cell processes including
224 adhesion, migration, invasion including stress-induced signaling[72]. Vim IF’s (~10nm) distributed throughout the
225 cell by association with microtubules (tubulin, 24nm) regulating cell-migration, and microfilaments(actin, 7nm)
226 regulating cell-contractility, form the cytoskeletal network and provide mechanical support for the plasma

227 membrane where it contacts other cells or the extracellular matrix[73]. Interestingly, during the biological process
228 epithelial to mesenchymal transition wherein non-motile, polar epithelial cells transform to motile invasive non-
229 polar mesenchymal cells[74], cells also undergo a cytoskeletal reorganization that includes changes in cell-
230 membrane integrity, disassembly of junction proteins, increased stress-fiber formations, altered cell-surface
231 protein expression. Changes in the localization of proteins is a hallmark of this pathologic process. Our
232 observation that Vimentin is upregulated and translocated to the cell surface[75] in the early stages of tau
233 hyperphosphorylation suggests a possible role for EMT-related processes at the start of a slow progression
234 towards AD pathology.

235 While positron emission tomography (PET) is the mainstay of molecular imaging, and exhibits
236 remarkable sensitivity, there are several limitations posed by this methodology[62,76]. Access to PET imaging is
237 limited, even in the relatively well-served US, and is skewed towards high density urban centers. PET costs are
238 very high due to the need for same-day radiosynthesis, and rapid decay of the isotopes. Longer half-life isotopes
239 cause higher radiation exposure. This tradeoff between half-life and radiation exposure greatly limit the reach of
240 PET to a wider patient population. Current PET tau tracers recognize the tau β-sheets in the PHF and NFT
241 present in tauopathies[22]. This conformation is not unique to tau and the *in vivo* specificity is circumspect limiting
242 its interpretation. Off-target binding of Flortaucipir, an approved tau PET agent, has been reported since it binds
243 the MAO-B enzyme in the brain[77,78]. Further, the vast majority of pathological tau is actually intracellular, posing
244 a significant barrier to PET tracers that must navigate to the site of tau pathology, bind the target, and have all
245 unbound tracer molecules cleared from the brain before the radioactive signal decays. Our choice of MRI as the
246 detection modality is based on hyper-T1 relaxive properties of nanoparticles with surface conjugated Gd chelates,
247 bringing detection sensitivity to the same range as nuclear imaging, and the MRI agent does not suffer from the
248 rapid signal decay of PET agents, allowing plenty of time for unbound tracer to clear from the brain before
249 imaging. Our choice of a cell surface surrogate marker of tau hyperphosphorylation avoids the need to bind an
250 intracellular target. Finally, MRI imaging is already included in AD management and can be adjusted with agents
251 such as TauX nanoparticles to constitute a highly sensitive and specific test for future tau pathology.

252 In summary, our work shows that the hyperphosphorylative conditions coinciding with the initiation of a
253 decades long process culminating in AD result in markers manifested on the cell surface. By imaging their
254 presence, our approach detects the presence of hyperphosphorylative cells indicative of a presymptomatic stage

255 of AD. Coupled with early amyloid detection, this test could enable early positive diagnosis using the NIA-AA
256 research framework.

257 Materials and Methods

258 **Cell-lines -** SH-SY5Y cells (ATCC, Manassas, VA, #CRL-2266™) were obtained from Dr. Jason Shohet's lab at
259 the Texas Children's Hospital, Houston, immortalized human hepatocytes (THLE-3) were purchased from
260 American Type Culture Collection (ATCC, Manassas, VA, # CRL-11233™); both were cultured according to the
261 ATCC instructions. ReN cell™ VM (#SCC008) cultured as per instruction using neural stem cell maintenance
262 medium (#SCM005) and growth factors EGF (GF001) and bFGF(#GF005) all from Millipore Sigma, Burlington,
263 MA.

264 **Differentiation -** SH-SY5Y cells were exposed to 30 μM *all-trans*-Retionic acid (Sigma-Aldrich, St.Louis, MO, #
265 R2625) in serum free cell medium for 10 days with medium change every alternate day. ReNcell VM were
266 differentiated by the removal of growth factors from its culture medium for 10 days.

267 **Hyperphosphorylation -** was induced in SH-SY5Y cells by addition of 30 nM okadaic acid (Sigma Aldrich,
268 St.Louis, MO, # 459620) in growth medium with 30 μM RA for 24 hours. ReNcell VM were hyperphosphorylated
269 using 100nM Quinolinic Acid (SigmaAldrich, St.Louis, MO, #P63204) in culture media for 24h.

270 **Synthesis of primers and TA DNA library -** All primers and Cy5, and amine labelled selected aptamers were
271 purchased from Integrated DNA Technologies (IDT, Coralville, IA). The ssDNA library used in Cell-SELEX
272 contained a central randomized sequence of 30 nucleotides flanked by PCR primer regions to enable the PCR
273 amplification of the sequence (5'-CGCTCGATAGATCGAGCTTCG-$(N)_{30}$-GTCGATCACGCTCTAGAGCACTG-
274 3'). The chemically synthesized DNA library was converted to a phosphorothioate modified library by PCR
275 amplification using, dATP (αS), resulting in the DNA sequences where the 3' phosphate of each residue is
276 substituted with monothiophosphate groups, as described previously in detail [32,79]. The reverse primer was
277 labeled with biotin to separate the sense strand from the antisense strand by streptavidin-coated sepharose
278 beads (PureBiotech, Middlesex, NJ, # MSTR0510) for the next selection round. The concentration of the TA
279 library was determined with a NanoDrop™ 2000 by measuring the UV absorbance at 260 nm.

280 **Cell-SELEX -** The procedures of Cell-SELEX were performed according to protocol previously with some
281 modification [33,80].The initial ssDNA library of 150 pmole was dissolved in binding buffer with a total volume of 350

282 µl. It was denatured by heating at 95°C for 5 min, then renatured by rapid cooling on ice for 10 min. The treated
283 SH-SY5Y cells at approximately 90% confluence in a 100-mm culture plate were washed twice with washing
284 buffer and followed by incubating with the ssDNA library of 150 pmole for 2 hrs at 4°C. Following the incubation,
285 for positive selections, the supernatant was discarded, and cells were washed three times with washing buffer to
286 remove any unbound sequences. Then cells were scraped off and transferred to nuclease-free water, following
287 another three times nuclease-free water washes. Cells in nuclease-free water was centrifuged at 300×g for 5
288 min. QIAamp DNA Mini and Blood Mini kit (Qiagen, Germantown, MD, # 51104) was introduced to elute cell
289 membrane fraction. The cell membrane fraction was PCR-amplified to monitor the presence of cell binding
290 efficacy at each cycle. For negative selections, the supernatant was simply pipetted out of the flask and
291 processed for the next cycle of selection. The desired compartment were amplified by PCR, and used to prepare
292 the TA for the next round of selection. Two different negative selections were involved. One was differentiated
293 treatment only SH-SY5Y cells at cycles #12 and #13. Another was hepatocyte THLE-3 cells at cycles #20 and
294 #21. A total of 26 cycles of Cell-SELEX were conducted, including two different types of negative selections
295 mentioned above.

296 **Next-Generation Sequencing (NGS) -** At the studied cycles, the membrane fractions were isolated and the
297 recovered TA sequences were amplified by PCR. Equimolar quantities of the recovered TA sequences over the
298 range were pooled together and sequenced by Next-Gen DNA sequencing using Ion318 chip (ThermoFisher,
299 Waltham, MA). A four base sequence was introduced during PCR amplification to serve as unique "barcode" to
300 distinguish between the studied cycles. Sequencing results were analyzed by the Aptalinger [39] that uses the
301 markov model probability theory to find the optimal alignment of the sequences.

302 **Aptamer binding studies** – were conducted with undifferentiated, differentiated and hyperphosphorylated SH
303 SY5Y and ReN cell VM grown in 96-wells seeded at 10000 per well. The apparent dissociation constants (Kds)
304 were measured by the equation Y=Bmax X/ (Kd+X), with GraphPad Prism 9, San Diego, CA, with a saturation
305 binding experiment; cells were incubated with varying concentrations of Cy5-labeled aptamer in a 100 µl volume
306 of binding buffer containing cells, incubated for 30minutes, washed twice and resuspended in 100 µl buffer and
307 analyzed by Molecular probes microplate reader equipped with the appropriate excitation and emission filters.
308 All data points were collected in triplicate.

309 **Immunocytochemistry -** Eight-well glass plate was coated with a solution of 100 µg/ml Collagen Type I
310 (Thermofisher Scientific, Waltham, MA, # A1064401) dissolved in 0.01N HCl and air dried, then PBS washed

311 and air dried prior to seeding 20,000 SH-SY5Y cells per well. Aptamer staining at 100 nM was performed with
312 live cells for 2h at 4ºC in binding buffer and washed twice with washing buffer. Cells were then fixed by incubation
313 for 15 min in 4% formaldehyde in PBS at room temperature. Non-specific binding was blocked with blocking
314 buffer (G-Biosciences, St. Louis, MO, # 786195) for 1 hour and overnight incubation at 4°C with the rabbit pTau
315 primary antibody (1:100) (Santa Cruz Biotechnology, #: sc-101815) was followed by washing with PBS, and 1h
316 incubation with goat anti-rabbit IgG secondary antibody, Alexa Fluor 488 (Invitrogen, Carlsbad, CA, # A-11008)
317 for 1 hour at room temperature. Cytoskeletal actin filaments were stained with Alexa Fluor 594 Phalloidin
318 (Invitrogen, # A12381). The cells were covered with VECTASHIELD hardset mounting medium with DAPI (Vector
319 Laboratories, Burlingame, CA, # H-1500) for 5 min at room temperature. Images were visualized under Olympus
320 Fluoview FV1000 confocal microscopy.

321 **TauX nanoparticle synthesis –** L-α-phosphatidylcholine, hydrogenated (Hydro Soy PC; HSPC) and Cholesterol
322 were purchased from Lipoid Inc., Newark NJ, USA. 1,2-distearoyl-sn-glycero-3-phosphoethanolamine-N-
323 [methoxy(polyethylene glycol)-2000] (DSPE-mPEG2000) was purchased from Corden Pharma, Liestahl,
324 Switzerland. DSPE-PEG3400-COOH and Gd-DOTA-DSPE were synthesized *in house*, lis-rhodamine-DHPE
325 from ThermoFisher Scientific. HSPC, Cholesterol, DSPE-PEG3400-COOH, DSPE-mPEG2000, Gd-DOTA-
326 DSPE, lis-rhodamine-DHPE at molar proportions 31.4:40:0.5:3:25:0.1 were dissolved in ethanol to achieve a
327 total concentration of 100 mM. For the non-targeted control stealth liposomes, carboxy terminated PEG was not
328 included in the lipid mixture. The ethanolic solution of lipids was hydrated with 150mM saline solution at 65 °C
329 for 30 minutes, allowing multilamellar liposomes to form. The mixture was then extruded in a 10ml Lipex extruder
330 (Northern Lipids Inc., Burnaby, Canada) using a 400 nm polycarbonate track-etch polycarbonate filter (3 passes)
331 followed by a 200 nm (3 passes) and finally 100nM filters. The suspension was then diafiltered using a MicroKros
332 cross-flow diafiltration cartridge (*500 kDa* cutoff) from Repligen, Rancho Dominguez, CA, exchanging the external
333 buffer for phosphate buffered saline (PBS, pH 7.2) for 15 volume exchanges. To form the aptamer conjugated
334 liposomes, liposomes with lipid-PEG-COOH were reacted with amine terminated aptamers using carbodiimide
335 chemistry. The carboxyl groups on the liposomes were activated with 5 mM EDC and 10 mM sulfo-NHS at pH~6
336 for 5-10 minutes. The activated liposomes were then immediately reacted with the amine terminated aptamers
337 and the pH was raised to ~7.3 - 7.6 by titrating µl amounts of 5 N NaOH. The final concentration of aptamers
338 used in reaction is ~140 µM. The reaction was mixed at room temperature for 1 hr following which the reaction
339 was carried out at 4 deg ^{0}C overnight. The liposomes were then dialyzed against PBS to remove unconjugated

340 aptamers using a 300 kDa dialysis membrane. The dialysate (external phase) was concentrated using 10 kD
341 centrifugal separator and washed with PBS to remove residual EDC/s-NHS. The concentrated dialysate was
342 analysed by NanoDrop Spectrophotometer (ThermoFisher Sci., Waltham, MA, USA) to determine unconjugated
343 aptamer fraction, and estimate aptamer density per nanoparticle in TauX formulations. Inductively coupled
344 plasma atomic emission spectroscopy (ICP-AES) was used to measure Gd and phosphorus concentrations of
345 TauX formulations. The hydrodynamic diameter of liposomal nanoparticles in TauX formulations was determined
346 using a dynamic light scattering instrument.

347 **Mice –** All the procedures were performed with approval from Institutional Animal Care and Use Committee
348 (IACUC) of Baylor College of Medicine. Mice were kept under a 12 h light/dark cycle, with food and water available
349 ad libitum. PS19 mice from Jackson Laboratories (Bar Harbor, ME) B6; C3-Tg (Prnp-MAPT*P301S) PS19Vle/J
350 Stock No: 008169 were used and experiments were conducted at the 2m of age. The transgenic (TG) mice
351 develop neurofibrillary tangles by 5 months of age[64]. Age-matched non-transgenic wild type (WT) mice were
352 used as controls.

353 **Magnetic Resonance Imaging (MRI) -** MRI was performed on a 1T permanent magnet scanner (M7, Aspect
354 Imaging, Shoham, Israel). Mice underwent pre-contrast baseline scans. Thereafter, mice were intravenously
355 administered one of three nanoparticle MR contrast agents (TauT1, TauT3 or non-targeted control liposomes)
356 via tail vein at a dose of 0.20 mmol Gd/kg of body weight. Delayed post-contrast MRI was performed 4 days after
357 contrast agent injections. Pre-contrast and delayed post-contrast MR images were acquired using a T1-weighted
358 spin echo (T1w-SE) sequence and a fast spin echo inversion recovery (FSE-IR) sequence with the following
359 parameters: *SE parameters*: TR = 600 ms, TE = 11.5 ms, slice thickness = 1.2 mm, matrix = 192 × 192, FOV = 30
360 mm, slices = 16, NEX = 4; *FSE-IR parameters*: TR = 13500 ms, TE = 80 ms, TI = 2000 ms, slice thickness = 2.4
361 mm, matrix = 192 × 192, FOV = 30 mm, slices = 6, NEX = 6. Coil calibration, RF calibration, and shimming were
362 performed at the beginning of study for each subject. The pre-contrast scans provide a baseline for calculation
363 of signal enhancement from resulting post-contrast scans[46]. Two-standard deviations above the mean variation
364 within WT control animals was used as the cutoff signal intensity for identifying tau positive animals. Six
365 transgenic (TG) mice and six wild type mice (WT) were used for testing of each nanoparticle contrast agent
366 formulation. Receiver operating characteristic (ROC) curves were generated on a six point ordinal scale by
367 plotting the true positive fraction (TPF) against the false positive fraction (FPF) based on imaging-based
368 identification of Tau-positive animals using the cutoff signal intensity and then comparing against histological

369 confirmation of Tau pathology as a gold standard. A fitted curve was then generated against the empirical points
370 plotted on the graphs. Qualitative and quantitative analysis of MRI images was performed in OsiriX (version 5.8.5,
371 64-bit, Pixmeo SARL, Geneva, Switzerland) and MATLAB (version 2015a, MathWorks, Natick, MA).

372 **Immunofluorescence –** After the final MRI scan, the mice were euthanized and perfused extensively with 0.9%
373 saline followed by 4% paraformaldehyde for 15 mins. The brains were then immersion-fixed in 4% formaldehyde
374 for 48h at 4ºC, transferred to 30% sucrose for cryoprotection and embedded in OCT. Phenotypic confirmation for
375 the presence of phosphorylated tau and vimentin was done on 25µm thick brain sections. Antigen retrieval in
376 pH=8.5 citrate buffer was executed in a 1200W GE microwave for 15mins. After 15 minutes of cooling 25µL of
377 1:50 dilution of primary p-tau antibody namely either AT8,AT100 or AT180 that recognize different p-tau species
378 were incubated in a tray (RPI, Mt. Prospect, IL #248270) designed for microwave enhanced immunostaining
379 procedures for 3min at power level 3. After a 2 min cooling, sections were washed with PBS and incubated for
380 3min with a 1:100 dilution of appropriate secondary antibody. DAPI staining proceeded after 2 mins of cooling
381 and a PBS washing. ProGold Antifade (Invitrogen, Carlsbad, CA, # P36030) was used to mount slides which
382 were visualized on Olympus Fluoview LV100. Scanning of whole sections was also conducted using a Biotek
383 Cytation 5 slide scanning microscope. List of Antibodies – AT8 (#MN1020), Vimentin SP20 (#MA516409) both
384 Thermo Fisher Scientific, Waltham, MA, Vimentin D21H3 (Cell Signaling Technology, Beverly, MA, #5741T,),
385 Cell-surface vimentin (Abnova, Taipei City, Taiwan, #H00007431-M08J).

386 **Target Identification -** The protein targets of Tau-1, Tau-3, Tau-4 and Tau-5 were identified by affinity-pull down
387 using the selected aptamers as the capturing reagent followed by mass-spectroscopy. A scrambled DNA
388 sequence, R2, was used as a control. The hyperphosphorylated SH-SY5Y cells, at 90-95% confluence were
389 washed with cold PBS buffer and incubated with biotinylated selected aptamers with 25mmol/l each at 4°C in
390 PBS, respectively. After 2 hours of gentle agitation, SH-SY5Y cells were cross-linked with 1% formaldehyde for
391 10 minutes at room temperature. The formaldehyde cross-linking was quenched with glycine. Cells were scraped
392 from the plate, washed and lysed with lysing buffer (Thermofisher Scientific, # 87787) and treated with protease
393 inhibitor mixture. The lysates were freeze-thawed for 30 minutes on ice and cleared by centrifuging at 10,000 ×g
394 for 2 minutes at 4°C. To pull down the cross-linked proteins, equal amounts of cell lysate were incubated with
395 prewashed streptavidin magnetic beads for 1 hour at room temperature with continuous rotation. Protein
396 digestions were performed on the beads to isolate targeted proteins and processed for mass spectrometric
397 analysis. Each sample was analyzed in triplicates. The raw data files were processed to generate a Mascot

398 Generic Format with Mascot Distiller and searched against the SwissProt_2012_01 (Human) database using the
399 licensed Mascot search engine v2.3.02 (Matrix Science, Boston, MA) run on an in-house server.

400 **References**

401 1. Goedert, M., Wischik, C. M., Crowther, R. A., Walker, J. E. & Klug, A. Cloning and sequencing of
402 the cDNA encoding a core protein of the paired helical filament of Alzheimer disease: identification
403 as the microtubule-associated protein tau. *Proc. Natl. Acad. Sci. U. S. A.* **85**, 4051–4055 (1988).

404 2. Goedert, M., Spillantini, M. G., Jakes, R., Rutherford, D. & Crowther, R. A. Multiple isoforms of
405 human microtubule-associated protein tau: sequences and localization in neurofibrillary tangles of
406 Alzheimer's disease. *Neuron* **3**, 519–526 (1989).

407 3. Iqbal, K., Liu, F. & Gong, C. Tau and neurodegenerative disease: the story so far. *Nat. Rev.*
408 *Neurol.* **12**, 15–27 (2016).

409 4. Guo, T., Noble, W. & Hanger, D. Roles of tau protein in health and disease. *Acta Neuropathol.*
410 **133**, 665–704 (2017).

411 5. Wang, Y. & Mandelkow, E. Tau in physiology and pathology. *Nat. Rev. Neurosci.* **17**, 22 (2016).

412 6. Chong, F. P., Ng, K. Y., Koh, R. Y. & Chye, S. M. Tau Proteins and Tauopathies in Alzheimer's
413 Disease. *Cell. Mol. Neurobiol.* **38**, 965–980 (2018).

414 7. Karikari, T. K. *et al.* Distinct conformations, aggregation and cellular internalization of different tau
415 strains. *Front. Cell. Neurosci.* **13**, 1–16 (2019).

416 8. d'Errico, P. & Meyer-Luehmann, M. Mechanisms of Pathogenic Tau and Aβ Protein Spreading in
417 Alzheimer's Disease. *Front. Aging Neurosci.* **12**, 1–10 (2020).

418 9. Brunello, C. A., Merezhko, M., Uronen, R. L. & Huttunen, H. J. Mechanisms of secretion and
419 spreading of pathological tau protein. *Cell. Mol. Life Sci.* **77**, 1721–1744 (2020).

420 10. Vogel, J. W. *et al.* Spread of pathological tau proteins through communicating neurons in human
421 Alzheimer's disease. *Nat. Commun.* **11**, 2612 (2020).

422 11. Gibbons, G. S., Lee, V. M. Y. & Trojanowski, J. Q. Mechanisms of Cell-to-Cell Transmission of
423 Pathological Tau: A Review. *JAMA Neurol.* **76**, 101–108 (2019).

424 12. Jack Jr, C. R. *et al.* NIA-AA research framework: toward a biological definition of Alzheimer's
425 disease. *Alzheimer's Dement.* **14**, 535–562 (2018).

426 13. Jack, C. R. *et al.* A/T/N: an unbiased descriptive classification scheme for Alzheimer disease
427 biomarkers. *Neurology* **87**, 539–547 (2016).

428 14. Selkoe, D. J. & Hardy, J. The amyloid hypothesis of Alzheimer's disease at 25 years. *EMBO Mol.*
429 *Med.* **8**, 595–608 (2016).

430 15. Mattsson-Carlgren, N. *et al.* Aβ deposition is associated with increases in soluble and
431 phosphorylated tau that precede a positive Tau PET in Alzheimer's disease. *Sci. Adv.* **6**, (2020).

432 16. Leuzy, A. *et al.* Longitudinal tau and metabolic PET imaging in relation to novel CSF tau measures
433 in Alzheimer's disease. *Eur. J. Nucl. Med. Mol. Imaging* **46**, 1152–1163 (2019).

434 17. Cummings, J. L. Biomarkers in Alzheimer's disease drug development. *Alzheimer's Dement.* **7**,
435 e13–e44 (2011).

436 18. Smoler, M., Coceano, G., Testa, I., Bruno, L. & Levi, V. Apparent stiffness of vimentin intermediate
437 filaments in living cells and its relation with other cytoskeletal polymers. *Biochim. Biophys. Acta -*
438 *Mol. Cell Res.* **1867**, 118726 (2020).

439 19. Peskind, E., Nordberg, A., Darreh-Shori, T. & Soininen, H. Safety of lumbar puncture procedures
440 in patients with Alzheimer's disease. *Curr. Alzheimer Res.* **6**, 290–292 (2009).

441 20. Wittenberg, R., Knapp, M., Karagiannidou, M., Dickson, J. & Schott, J. M. Economic impacts of
442 introducing diagnostics for mild cognitive impairment Alzheimer's disease patients. *Alzheimer's*
443 *Dement. Transl. Res. Clin. Interv.* **5**, 382–387 (2019).

444 21. Ehman, E. C. *et al.* PET/MRI: where might it replace PET/CT? *J. Magn. Reson. Imaging* **46**, 1247–
445 1262 (2017).

446 22. Leuzy, A. *et al.* Tau PET imaging in neurodegenerative tauopathies—still a challenge. *Mol.*
447 *Psychiatry* **24**, 1112–1134 (2019).

448 23. Jack Jr, C. R. *et al.* Tracking pathophysiological processes in Alzheimer's disease: an updated
449 hypothetical model of dynamic biomarkers. *Lancet Neurol.* **12**, 207–216 (2013).

450 24. Terry, R. D. *et al.* Physical basis of cognitive alterations in Alzheimer's disease: synapse loss is
451 the major correlate of cognitive impairment. *Ann. Neurol. Off. J. Am. Neurol. Assoc. Child Neurol.*
452 *Soc.* **30**, 572–580 (1991).

453 25. Hyman, B. T. *et al.* National Institute on Aging–Alzheimer's Association guidelines for the
454 neuropathologic assessment of Alzheimer's disease. *Alzheimer's Dement.* **8**, 1–13 (2012).

455 26. Montine, T. J. *et al.* National Institute on Aging–Alzheimer's Association guidelines for the
456 neuropathologic assessment of Alzheimer's disease: a practical approach. *Acta Neuropathol.* **123**,
457 1–11 (2012).

458 27. Wang, J.-Z., Xia, Y.-Y., Grundke-Iqbal, I. & Iqbal, K. Abnormal hyperphosphorylation of tau: sites,
459 regulation, and molecular mechanism of neurofibrillary degeneration. *J. Alzheimer's Dis.* **33**,
460 S123–S139 (2013).

461 28. Grundke-Iqbal, I. *et al.* Abnormal phosphorylation of the microtubule-associated protein tau (tau) in
462 Alzheimer cytoskeletal pathology. *Proc. Natl. Acad. Sci.* **83**, 4913–4917 (1986).

463 29. Delobel, P. *et al.* Analysis of tau phosphorylation and truncation in a mouse model of human
464 tauopathy. *Am. J. Pathol.* **172**, 123–131 (2008).

465 30. Lund, E. T., McKenna, R., Evans, D. B., Sharma, S. K. & Mathews, W. R. Characterization of the
466 in vitro phosphorylation of human tau by tau protein kinase II (cdk5/p20) using mass spectrometry.
467 *J. Neurochem.* **76**, 1221–1232 (2001).

468 31. Liu, F., Grundke-Iqbal, I., Iqbal, K. & Gong, C. Contributions of protein phosphatases PP1, PP2A,
469 PP2B and PP5 to the regulation of tau phosphorylation. *Eur. J. Neurosci.* **22**, 1942–1950 (2005).

470 32. Mu, Q. *et al.* Conjugate-SELEX: A High-throughput Screening of Thioaptamer-liposomal

471 Nanoparticle Conjugates for Targeted Intracellular Delivery of Anticancer Drugs. *Mol. Ther. -*
472 *Nucleic Acids* **5**, e382 (2016).

473 33. Parekh, P., Tang, Z., Turner, P. C., Moyer, R. W. & Tan, W. Aptamers Recognizing Glycosylated
474 Hemagglutinin Expressed on the Surface of Vaccinia Virus-Infected Cells. *Anal. Chem.* **82**, 8642–
475 8649 (2010).

476 34. Ayyagari, A. L. *et al.* Long-circulating liposomal contrast agents for magnetic resonance imaging.
477 *Magn. Reson. Med. An Off. J. Int. Soc. Magn. Reson. Med.* **55**, 1023–1029 (2006).

478 35. Kamat, P. K., Rai, S., Swarnkar, S., Shukla, R. & Nath, C. Molecular and Cellular Mechanism of
479 Okadaic Acid (OKA)-Induced Neurotoxicity: A Novel Tool for Alzheimer's Disease Therapeutic
480 Application. *Mol. Neurobiol.* **50**, 852–865 (2014).

481 36. Gulaj, E., Pawlak, K., Bien, B. & Pawlak, D. Kynurenine and its metabolites in Alzheimer's disease
482 patients. *Adv. Med. Sci.* **55**, 204–211 (2010).

483 37. The UniProt Consortium. UniProt: the universal protein knowledgebase in 2021. *Nucleic Acids*
484 *Res.* **49**, D480–D489 (2021).

485 38. Rothberg, J. M. *et al.* An integrated semiconductor device enabling non-optical genome
486 sequencing. *Nature* **475**, 348–352 (2011).

487 39. Lu, E., Elizondo-Riojas, M.-A., Chang, J. T. & Volk, D. E. Aptaligner: automated software for
488 aligning pseudorandom DNA X-aptamers from next-generation sequencing data. *Biochemistry* **53**,
489 3523–3525 (2014).

490 40. Katoh, K., Rozewicki, J. & Yamada, K. D. MAFFT online service: multiple sequence alignment,
491 interactive sequence choice and visualization. *Brief. Bioinform.* **20**, 1160–1166 (2019).

492 41. Sievers, F. *et al.* Fast, scalable generation of high-quality protein multiple sequence alignments
493 using Clustal Omega. *Mol. Syst. Biol.* **7**, 539 (2011).

494 42. Zuker, M. Mfold web server for nucleic acid folding and hybridization prediction. *Nucleic Acids*
495 *Res.* **31**, 3406–3415 (2003).

496 43. Donato, R. *et al.* Differential development of neuronal physiological responsiveness in two human
497 neural stem cell lines. *BMC Neurosci.* **8**, 1–11 (2007).

498 44. Ghaghada, K., Hawley, C., Kawaji, K., Annapragada, A. & Mukundan Jr, S. T1 relaxivity of core-
499 encapsulated gadolinium liposomal contrast agents—effect of liposome size and internal
500 gadolinium concentration. *Acad. Radiol.* **15**, 1259–1263 (2008).

501 45. Ghaghada, K. B. *et al.* New Dual Mode Gadolinium Nanoparticle Contrast Agent for Magnetic
502 Resonance Imaging. *PLoS One* **4**, e7628 (2009).

503 46. Badachhape, A. A. *et al.* Pre-clinical dose-ranging efficacy, pharmacokinetics, tissue
504 biodistribution, and toxicity of a targeted contrast agent for MRI of amyloid deposition in
505 Alzheimer's disease. *Sci. Rep.* **10**, 16185 (2020).

506 47. Mattsson, N., Lönneborg, A., Boccardi, M., Blennow, K. & Hansson, O. Clinical validity of
507 cerebrospinal fluid Aβ42, tau, and phospho-tau as biomarkers for Alzheimer's disease in the
508 context of a structured 5-phase development framework. *Neurobiol. Aging* **52**, 196–213 (2017).

509 48. Coch, R. A. & Leube, R. E. Intermediate filaments and polarization in the intestinal epithelium.
510 *Cells* **5**, 32 (2016).

511 49. Cuingnet, R. *et al.* Automatic classification of patients with Alzheimer's disease from structural
512 MRI: a comparison of ten methods using the ADNI database. *Neuroimage* **56**, 766–781 (2011).

513 50. Johansson, M. *et al.* Mild behavioral impairment and its relation to tau pathology in preclinical
514 Alzheimer's disease. *Transl. Psychiatry* **11**, 1–8 (2021).

515 51. Suárez-Calvet, M. *et al.* Novel tau biomarkers phosphorylated at T181, T217 or T231 rise in the
516 initial stages of the preclinical Alzheimer's continuum when only subtle changes in Aβ pathology
517 are detected. *EMBO Mol. Med.* **12**, e12921 (2020).

518 52. Mattsson, N. *et al.* 18 F-AV-1451 and CSF T-tau and P-tau as biomarkers in Alzheimer's disease
519 . *EMBO Mol. Med.* **9**, 1212–1223 (2017).

520 53. Chung, S.-H. Aberrant phosphorylation in the pathogenesis of Alzheimer's disease. *BMB Rep.* **42**,

521 467–474 (2009).

522 54. Oliveira, J., Costa, M., de Almeida, M. S. C., da Cruz e Silva, O. A. B. & Henriques, A. G. Protein
523 phosphorylation is a key mechanism in Alzheimer's disease. *J. Alzheimer's Dis.* **58**, 953–978
524 (2017).

525 55. Augustinack, J. C., Schneider, A., Mandelkow, E.-M. & Hyman, B. T. Specific tau phosphorylation
526 sites correlate with severity of neuronal cytopathology in Alzheimer's disease. *Acta Neuropathol.*
527 **103**, 26–35 (2002).

528 56. Wang, Y. & Mandelkow, E. Tau in physiology and pathology. *Nat. Rev. Neurosci.* **17**, 22–35
529 (2016).

530 57. Wang, J., Grundke-Iqbal, I. & Iqbal, K. Kinases and phosphatases and tau sites involved in
531 Alzheimer neurofibrillary degeneration. *Eur. J. Neurosci.* **25**, 59–68 (2007).

532 58. Sontag, J.-M. & Sontag, E. Protein phosphatase 2A dysfunction in Alzheimer's disease. *Front.*
533 *Mol. Neurosci.* **7**, 16 (2014).

534 59. Sontag, J. M., Nunbhakdi-Craig, V., White, C. L., Halpain, S. & Sontag, E. The protein
535 phosphatase PP2A/Bα binds to the microtubule-associated proteins Tau and MAP2 at a motif also
536 recognized by the kinase Fyn: Implications for tauopathies. *J. Biol. Chem.* **287**, 14984–14993
537 (2012).

538 60. Franzmeier, N. *et al.* Functional brain architecture is associated with the rate of tau accumulation
539 in Alzheimer's disease. *Nat. Commun.* **11**, 1–17 (2020).

540 61. DeVos, S. L. *et al.* Synaptic tau seeding precedes tau pathology in human Alzheimer's disease
541 brain. *Front. Neurosci.* **12**, 267 (2018).

542 62. Dustin, D., Hall, B. M., Annapragada, A. & Pautler, R. G. Neuroimaging in Alzheimer's disease:
543 preclinical challenges toward clinical efficacy. *Transl. Res.* **175**, 37–53 (2016).

544 63. Takeuchi, H. *et al.* P301S mutant human tau transgenic mice manifest early symptoms of human
545 tauopathies with dementia and altered sensorimotor gating. *PLoS One* **6**, e21050 (2011).

546 64. Yoshiyama, Y. *et al.* Synapse loss and microglial activation precede tangles in a P301S tauopathy
547 mouse model. *Neuron* **53**, 337–351 (2007).

548 65. Holmes, B. B. *et al.* Proteopathic tau seeding predicts tauopathy in vivo. *Proc. Natl. Acad. Sci.*
549 **111**, E4376 LP-E4385 (2014).

550 66. Eriksson, J. E. *et al.* Introducing intermediate filaments: from discovery to disease. *J. Clin. Invest.*
551 **119**, 1763–1771 (2009).

552 67. Sihag, R. K., Inagaki, M., Yamaguchi, T., Shea, T. B. & Pant, H. C. Role of phosphorylation on the
553 structural dynamics and function of types III and IV intermediate filaments. *Exp. Cell Res.* **313**,
554 2098–2109 (2007).

555 68. Snider, N. T. & Omary, M. B. Post-translational modifications of intermediate filament proteins:
556 mechanisms and functions. *Nat. Rev. Mol. Cell Biol.* **15**, 163–177 (2014).

557 69. Battaglia, R. A., Delic, S., Herrmann, H. & Snider, N. T. Vimentin on the move: New developments
558 in cell migration [version 1; referees: 2 approved]. *F1000Research* **7**, 1–10 (2018).

559 70. Pattabiraman, S. *et al.* Vimentin protects differentiating stem cells from stress. *Sci. Rep.* **10**, 1–15
560 (2020).

561 71. Etienne-Manneville, S. Cytoplasmic Intermediate Filaments in Cell Biology. *Annu. Rev. Cell Dev.*
562 *Biol.* **34**, 1–28 (2018).

563 72. Ivaska, J., Pallari, H.-M., Nevo, J. & Eriksson, J. E. Novel functions of vimentin in cell adhesion,
564 migration, and signaling. *Exp. Cell Res.* **313**, 2050–2062 (2007).

565 73. Jones, J. C. R. *et al.* Intermediate filaments and the plasma membrane. *Cold Spring Harb.*
566 *Perspect. Biol.* **9**, (2017).

567 74. Kalluri, R. EMT: when epithelial cells decide to become mesenchymal-like cells. *J. Clin. Invest.*
568 **119**, 1417–1419 (2009).

569 75. Ivaska, J. Vimentin: Central hub in EMT induction? *Small GTPases* **2**, 1436–1448 (2011).

570 76. Hameed, S. *et al.* Role of Fluid Biomarkers and PET Imaging in Early Diagnosis and its Clinical
571 Implication in the Management of Alzheimer's Disease. *J. Alzheimer's Dis. Reports* **4**, 21–37
572 (2020).

573 77. Lemoine, L. *et al.* Comparative binding properties of the tau PET tracers THK5117, THK5351,
574 PBB3, and T807 in postmortem Alzheimer brains. *Alzheimers. Res. Ther.* **9**, 1–13 (2017).

575 78. Baker, S. L., Harrison, T. M., Maass, A., La Joie, R. & Jagust, W. J. Effect of off-target binding on
576 18F-Flortaucipir variability in healthy controls across the life span. *J. Nucl. Med.* **60**, 1444–1451
577 (2019).

578 79. Volk, D. E. & Lokesh, G. L. R. Development of phosphorothioate DNA and DNA thioaptamers.
579 *Biomedicines* **5**, 41 (2017).

580 80. Mu, Q. *et al.* Conjugate-SELEX: A high-throughput screening of thioaptamer-liposomal
581 nanoparticle conjugates for targeted intracellular delivery of anticancer drugs. *Mol. Ther. Acids* **5**,
582 e382 (2016).

583

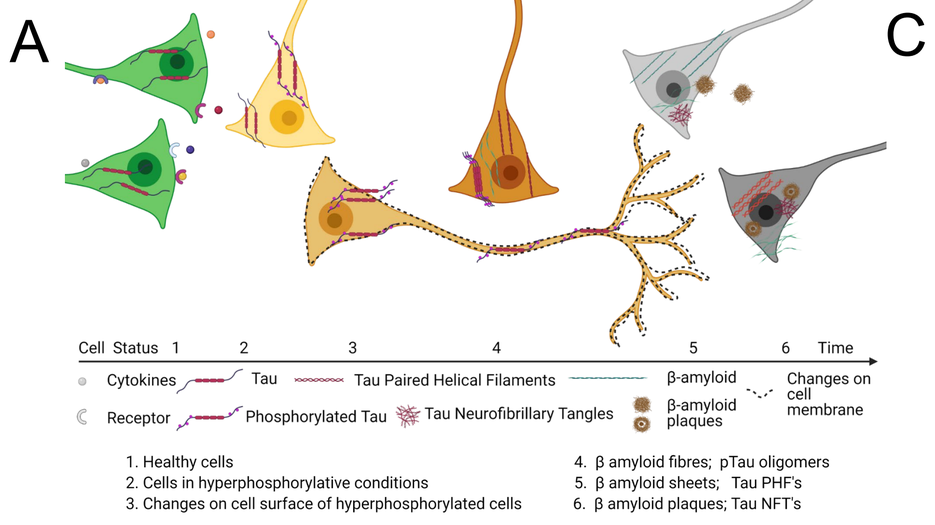

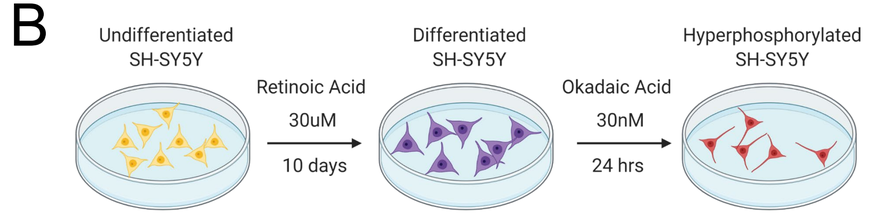

Figure 1: Hyperphosphorylation and cell surface changes in a cell of neuronal phenotype. (A) *Cell changes during hyperphosphorylation*: Tau hyperphosphorylation is a precursor to tau fibrillation. We hypothesize that cell surface changes occur in parallel with tau hyperphosphorylation. These changes may constitute a marker for early detection of AD. **(B)** *In vitro model of hyperphosphorylation in a cell of neuronal phenotype*: Differentiated SH-SY5Y cells are used to model hyperphosphorylation. Hyperphosphorylation can be induced by either okadaic acid (OA) or quinolinic acid (QA) **(C)** *Protein analysis at different stages of hyperphosphorylation*: Reverse phase protein array analysis of undifferentiated, retinoic acid (RA) differentiated and hyperphosphorylative cells (by Okadaic acid OA or Quinolinic acid QA). Heat map depicts changes in total protein expression. Proteins expressed on cell-membrane are depicted in red, peripheral –membrane proteins in blue and single-pass and multipass membrane proteins in green. Panel i) depicts changes in un-phosphorylated proteins on undifferentiated and ii) differentiated SH-SY5Y cells. Changes due to phosphorylation treatments with OA and QA on differentiated cells are shown in panels iii) undifferentiated and iv) differentiated SH-SY5Y cells

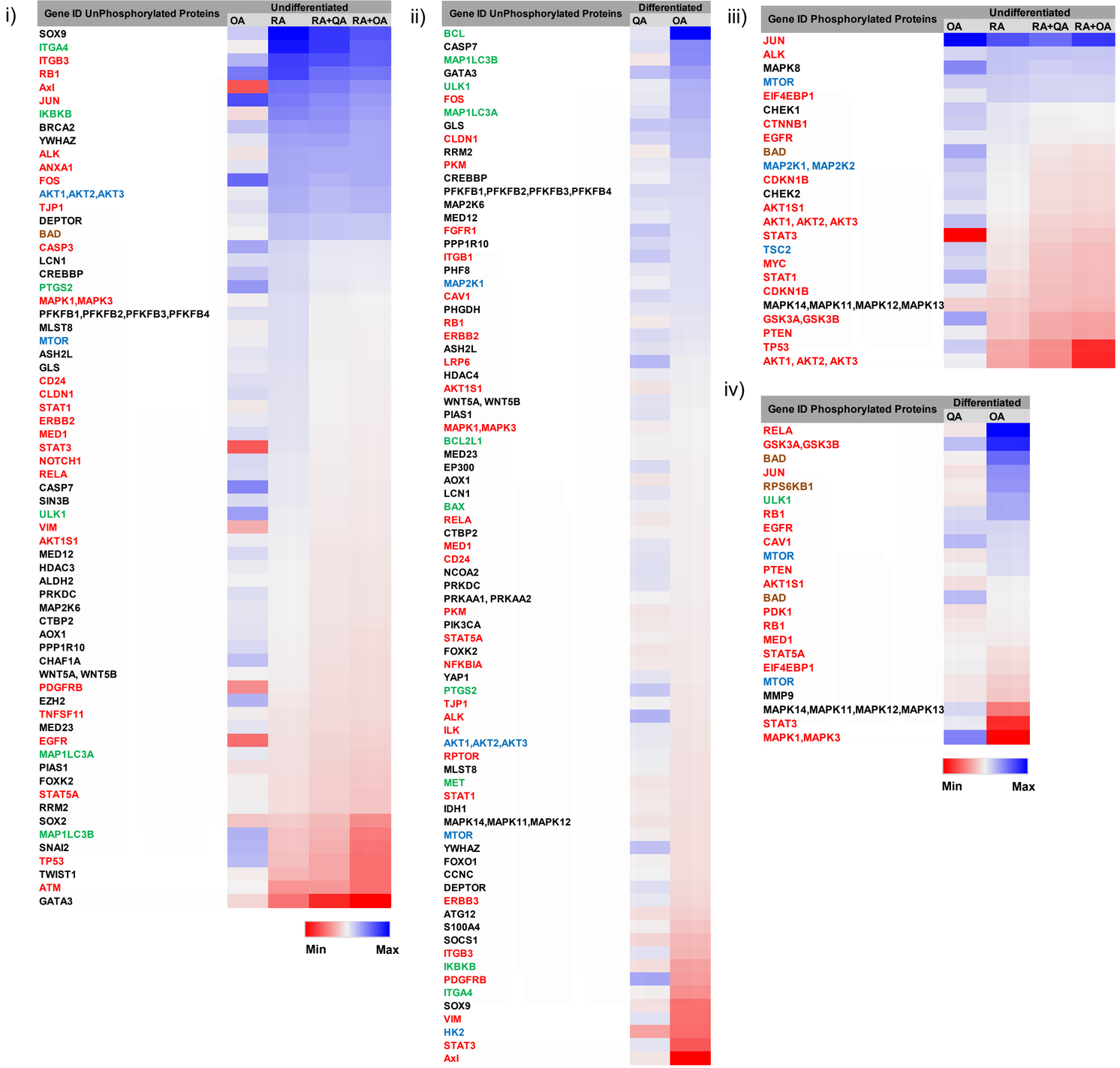

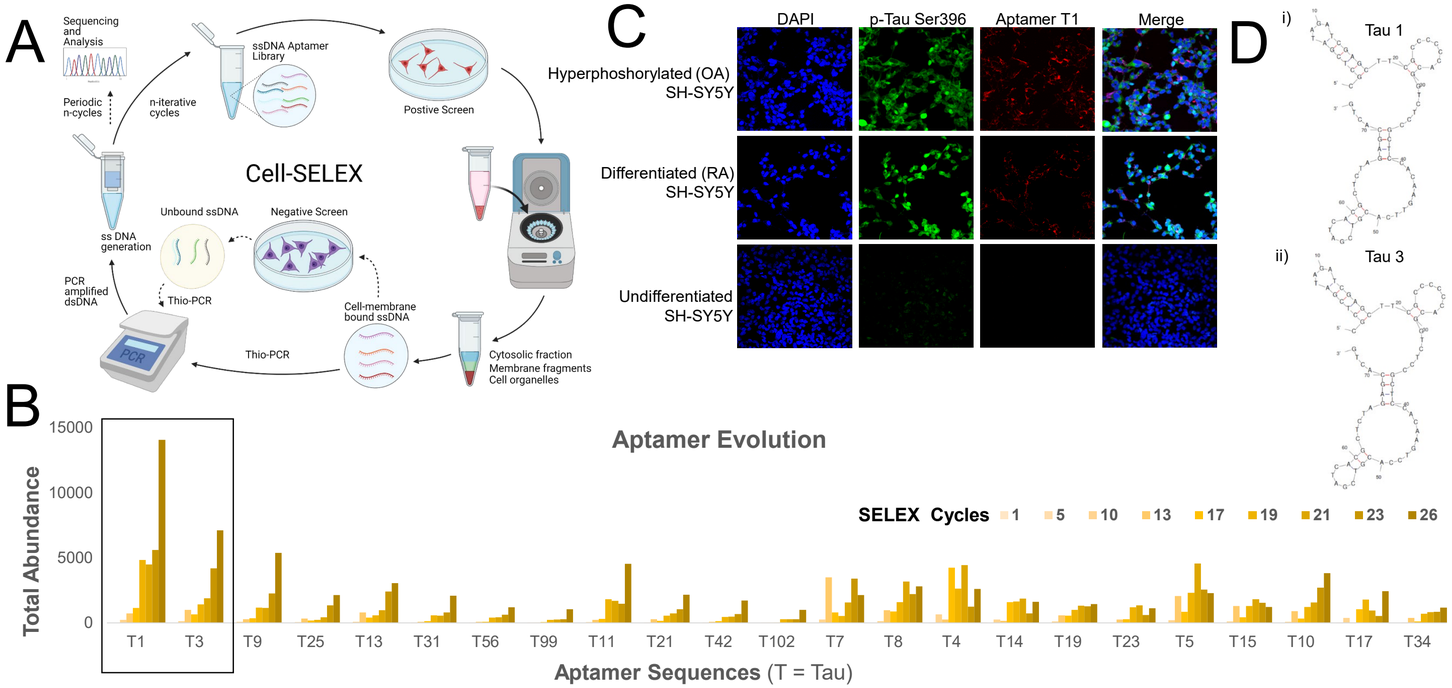

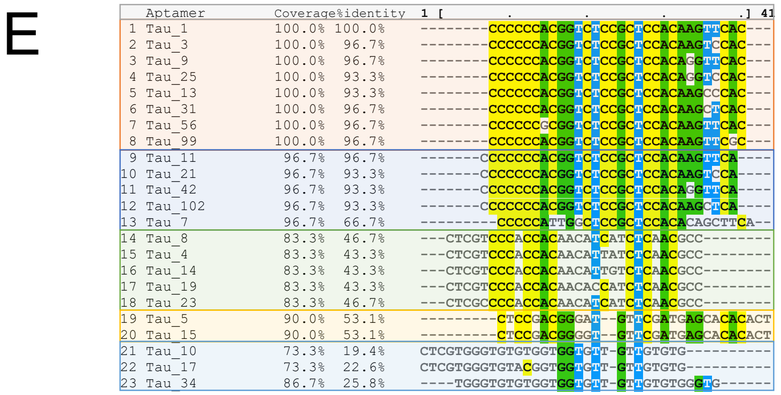

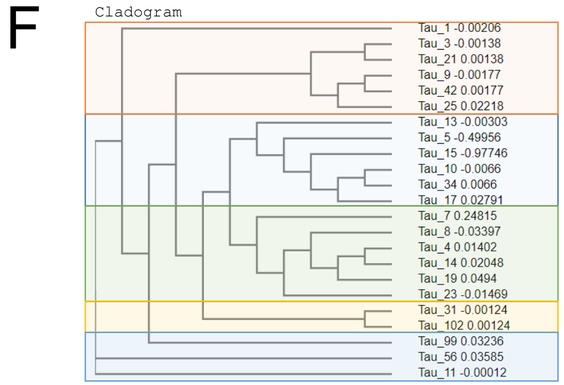

Figure 2: Cell-SELEX to identify biomarkers onset of AD. Okadaic acid treated differentiated SH-SY5Y cells were used as a surrogate for hyperphosphorylative neurons to screen DNA aptamers that specifically recognize the differences between the surfaces of treated and untreated cells, using the cell-SELEX methodology modified to capture membrane binding aptamers. (A) Pictorial representation of the cell-SELEX process (B) Abundance of the top 23 sequences from SELEX cycle 1 - 26 depicting their evolution. Note that the fractions are low until about cycle 10, when they increase sharply. Note that the abundance of Tau 1, Tau 3 continually increase with increasing cycle number. (C) Undifferentiated, differentiated (RA) and hyperphosphorylated (OA) SH-SY5Y cells stained with 50nM Cy5 labelled Tau1 aptamer for 2h at 4ºC. (D) i) Tau 1 and ii) Tau 3 secondary structure using Mfold. (E) Multiple sequence alignment of the top 23 aptamer sequences by MAFFT. Note the existence of five families. (F) Cladograms showing relationship between the Tau aptamer sequences and the aptamer families.

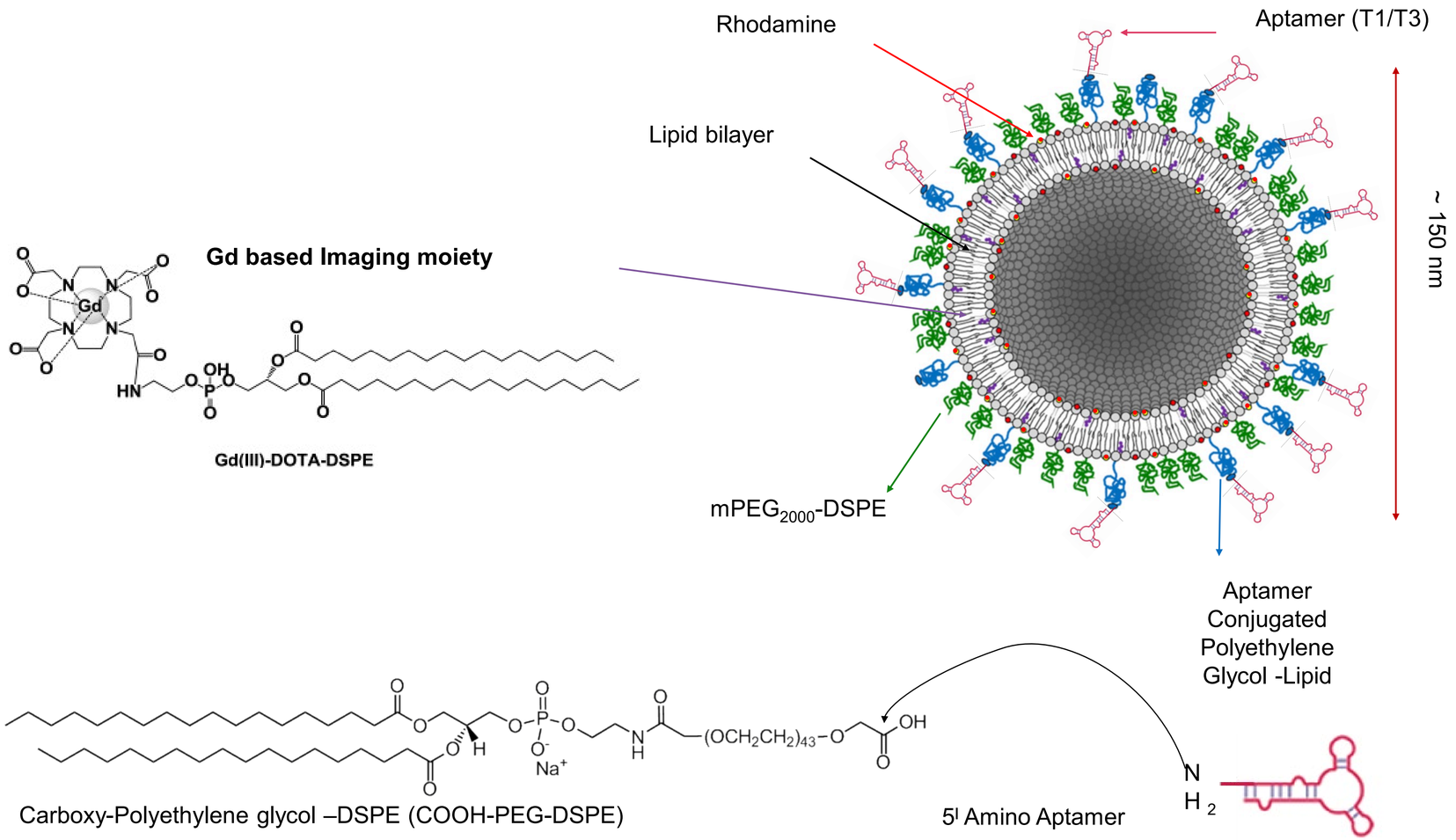

Figure 3: Aptamer-targeted liposomal-Gd nanoparticle TauX contrast agent. The liposomal bilayer incorporates DSPE-DOTA-Gd for MR contrast, DSPE-PEG2000 to enhance circulation half-life, DSPE-PEG3400-aptamer (Tau1/Tau3) for targeting and lissamine rhodamine for fluorescence imaging.

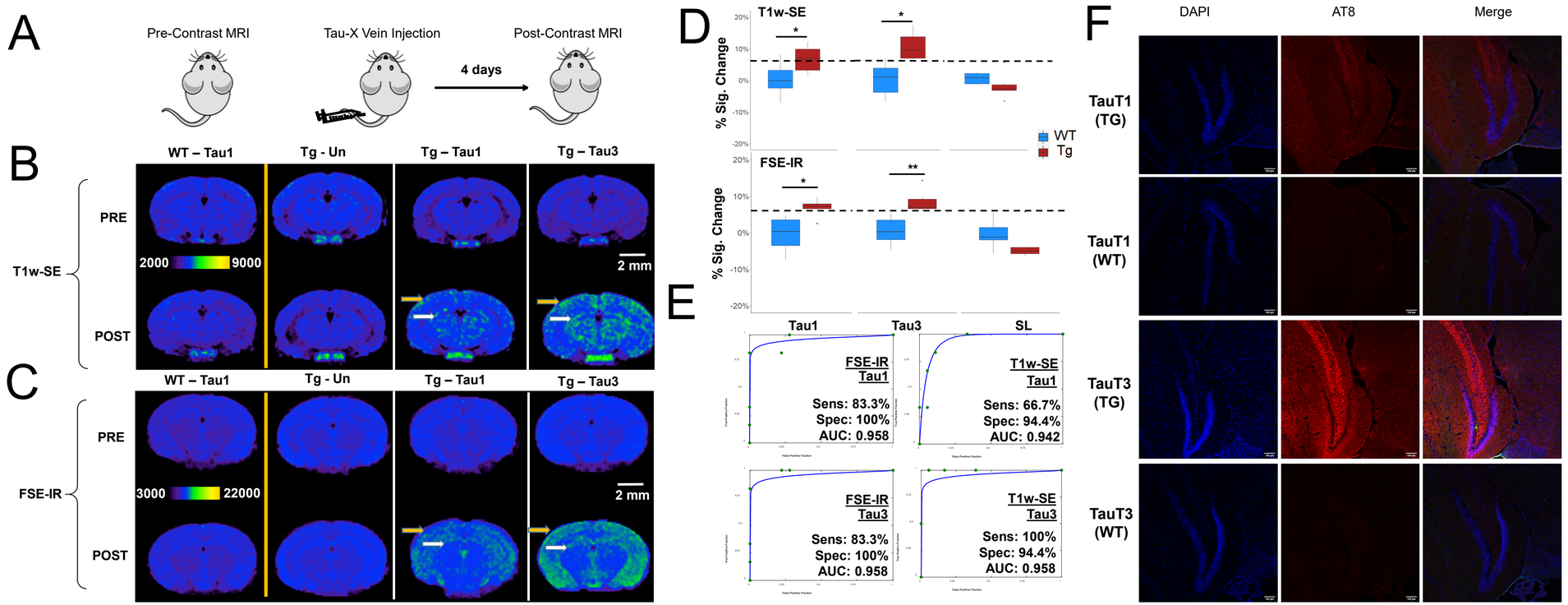

Figure 4: T1-weighted spin-echo (T1w-SE) and (FSE-IR) images demonstrate signal enhancement as TauX binds to hyperphosphorylated tau *in vivo*. (A) In vivo imaging was performed on a 1 T permanent MRI scanner (M7, Aspect Imaging). Two month old mice were injected with 0.2mM Gd dose TauX NP. Pre- and post-contrast images were acquired with the following parameters: Imaging sequence: T1 weighted spin echo (T1w-SE) TR = 600 ms, TE = 11.5 ms, slice thickness = 1.2 mm, matrix = 192x192, FOV = 30 mm, slices = 16, NEX = 4. Animals were euthanized after final imaging session and brains harvested for post-mortem analysis. (**B**) and (**C**) demonstrate signal enhancement in delayed post-contrast scans of transgenic (Tg) P301S mice treated with TauX relative to age-matched controls. Wild type (WT) animal shows no signal enhancement four days after administration of TauX. Tg animal showed high enhancement in cortical (yellow arrow) and hippocampal regions (white arrow) four days after administration of TauX. Transgenic animal shows no signal enhancement four days after injection of untargeted contrast (UC). Scale bar represents 2 mm. All animals are shown on the same color scale. (**D**) Signal enhancement in TG animals relative to WT counterparts and UC-treated Tg animals for both T1w-SE and FSE-IR sequences (*$p<0.05$; **$p<0.005$). (**E**) The Receiver operating characteristic (ROC) curve demonstrates TauX accuracy in identifying early age Tg animals. ROC curve is generated by fitting observed operating points for true positive fraction versus false positive fraction (green dots) using a six point ordinal scale. A fitted curve (blue) connects the observed operating points. Area under curve (AUC) is calculated using the fitted curve. Sensitivity describes the true positive rate for Tg mice given TauX (n=6) while specificity is the true negative rate for WT mice given TauX (n=6), WT mice given UC Gd nanoparticle contrast (n=6), and Tg mice receiving UC Gd nanoparticle contrast (n=6). (F) The mice selected for TauX injection were genotyped which only revealed the presence of transgene. We confirmed the presence of hyperphosphorylated tau species in the mice by immunofluoscence on the brains sections harvested post MRI scans. Brains were perfused with heparin-PBS and fixed in OCT. IF with antibody AT8 probed for presence of ptau species provided high concordance with genotype confirming the presence of hyperphosphorylative conditions in the mice.

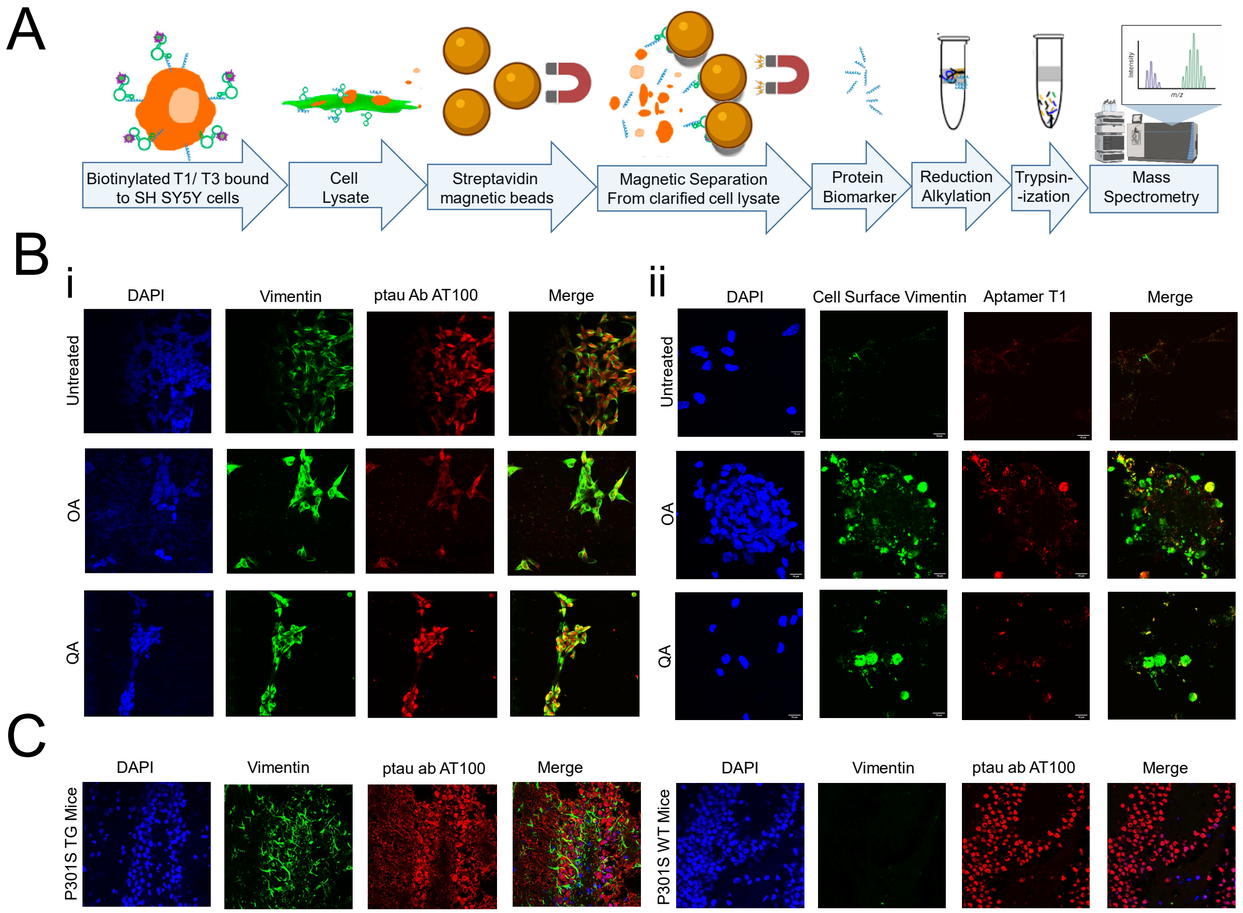

Figure 5: Proteomic analysis for aptamer target identification. A. Procedure for tryptic digest of aptamer bound cell membrane analyzed by LC/MS/MS. The raw data files were processed and searched against the SwissProt 2012 01 (Human) database. Vimentin was identified as possible target. B. Presence of the aptamers binding target on SH SY5Y cells; undifferentiated and hyperphosphorylated OA (24h, 30nM) and QA (24h, 100nM); i) co-stained with Vimentin (D21H3) and ptau (AT100) antibodies or ii) cell surface vimentin (Clone 84-1) antibody and aptamer T1 (50nM); nuclei counterstained with DAPI. C. Expression of Vimentin in P301S TG and WT frozen mouse tissue sections stained with Vimentin (SP20) and ptau (AT100) antibodies and DAPI stained nuclei.

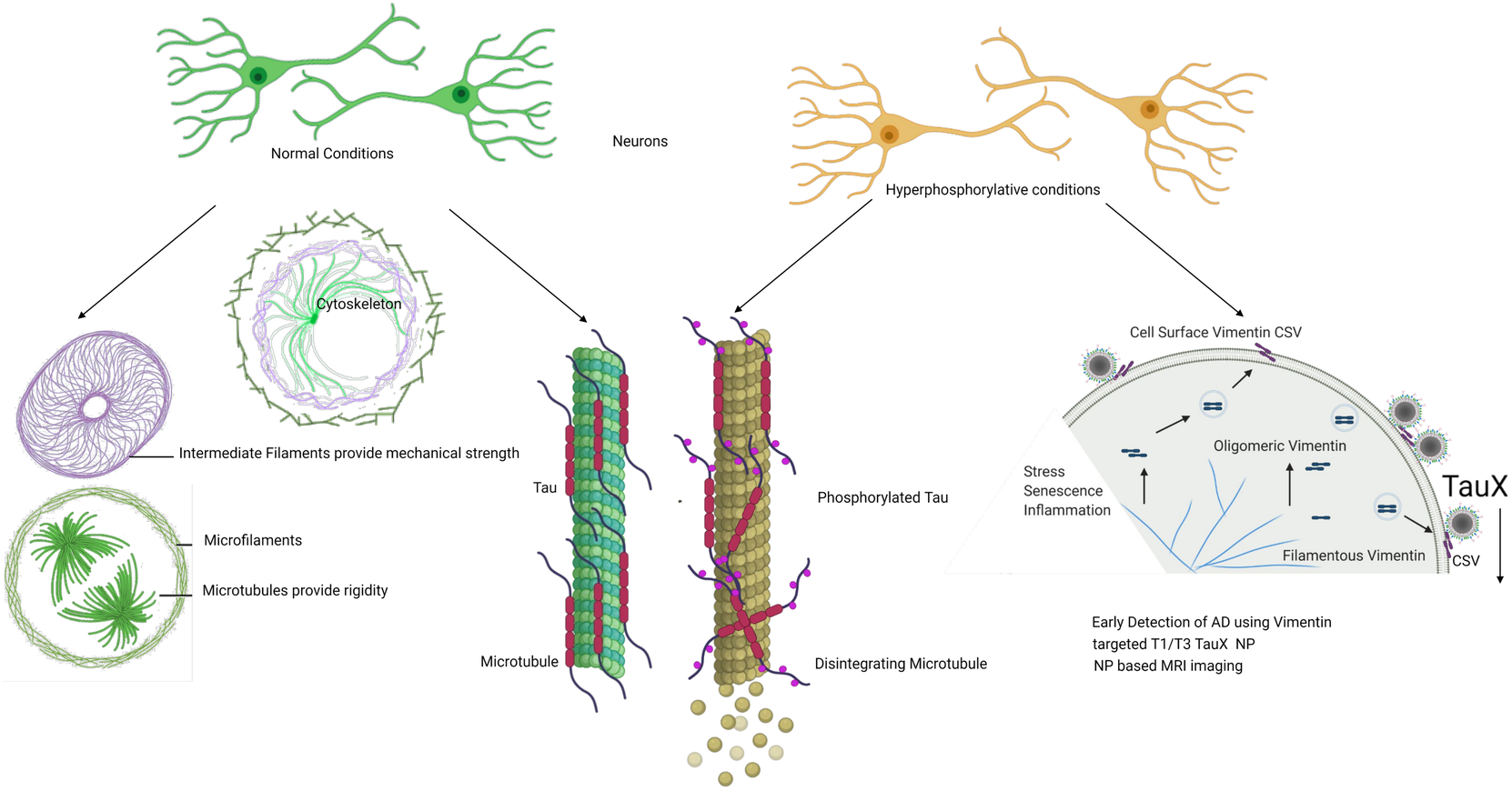

Figure 6: Early detection of AD. Hyperphosphorylative conditions provoke neuronal cells to undergo changes including on the cell surface. Translocation of Vimentin to the cell surface was exploited to generate an aptamer that was developed for *in vivo* use as targeted liposomal nanoparticle TauX for early MRI detection of tau pathology in a mouse model

It is NOT AD. AD is a human disease. This is a model of tau deposition. The scanner shown is a human scanner.

Supplementary Table 1: Target Identification using aptamer immunoprecipitation and mass spectrometry. The aptamer immunoprecipitation tryptic digest was purified with a ZipTip and analyzed by LC/MS/MS on an LTQ-Orbitrap-XLmass spectrometer (Thermo Fisher) interfaced with an EksigentNano-LC-Ultra-2D plus CHiPLC Nanoflex system (AB SCIEX). The raw data files were processed to generate a Mascot Generic Format with Mascot Distiller and searched against the SwissProt_2012_01 (Human) database using the licensed Mascot search engine v2.3.02(Matrix Science) run on an in-house server. Exponentially modified protein abundance index (emPAI) are reported in the table below that report protein content proportional to protein content in a mixture.

T1 emPAI	Target ID Aptamer T1
6.32	60 kDa heat shock protein, mitochondrial OS=Homo sapiens GN=HSPD1 PE=1 SV=2
3.49	Keratin, type II cytoskeletal 1 OS=Homo sapiens GN=KRT1 PE=1 SV=6
1.29	Keratin, type II cytoskeletal 2 epidermal OS=Homo sapiens GN=KRT2 PE=1 SV=2
0.38	Keratin, type II cytoskeletal 6B OS=Homo sapiens GN=KRT6B PE=1 SV=5
0.38	Keratin, type II cytoskeletal 6A OS=Homo sapiens GN=KRT6A PE=1 SV=3
0.11	Keratin, type II cytoskeletal 5 OS=Homo sapiens GN=KRT5 PE=1 SV=3
4.67	Keratin, type I cytoskeletal 10 OS=Homo sapiens GN=KRT10 PE=1 SV=6
1.66	Keratin, type I cytoskeletal 9 OS=Homo sapiens GN=KRT9 PE=1 SV=3
0.97	Keratin, type I cytoskeletal 14 OS=Homo sapiens GN=KRT14 PE=1 SV=4
0.69	Keratin, type I cytoskeletal 17 OS=Homo sapiens GN=KRT17 PE=1 SV=2
5.01	Single-stranded DNA-binding protein, mitochondrial OS=Homo sapiens GN=SSBP1 PE=1 SV=1
2.35	Actin, cytoplasmic 1 OS=Homo sapiens GN=ACTB PE=1 SV=1
0.13	Vimentin OS=Homo sapiens GN=VIM PE=1 SV=4
3.6	40S ribosomal protein S5 (Fragment) OS=Homo sapiens GN=RPS5 PE=1 SV=1
0.2	Microtubule-associated protein 1B OS=Homo sapiens GN=MAP1B PE=1 SV=2
1.27	Elongation factor 1-alpha 1 OS=Homo sapiens GN=EEF1A1 PE=1 SV=1
1.07	Cofilin 1 (Non-muscle), isoform CRA_a OS=Homo sapiens GN=CFL1 PE=1 SV=1
0.28	Leucine-rich PPR motif-containing protein, mitochondrial OS=Homo sapiens GN=LRPPRC PE=1 SV=3
2.74	Peptidyl-prolyl cis-trans isomerase B OS=Homo sapiens GN=PPIB PE=1 SV=2
2.35	Alpha-enolase OS=Homo sapiens GN=ENO1 PE=1 SV=2
0.61	Stress-70 protein, mitochondrial OS=Homo sapiens GN=HSPA9 PE=1 SV=2
1.91	ATP synthase subunit O, mitochondrial OS=Homo sapiens GN=ATP5O PE=1 SV=1
0.73	Serpin H1 OS=Homo sapiens GN=SERPINH1 PE=1 SV=2
0.53	ATP synthase subunit alpha, mitochondrial OS=Homo sapiens GN=ATP5A1 PE=1 SV=1
0.61	ATP synthase subunit gamma, mitochondrial OS=Homo sapiens GN=ATP5C1 PE=1 SV=1
0.94	Tubulin beta chain OS=Homo sapiens GN=TUBB PE=1 SV=1
0.97	Nascent polypeptide-associated complex subunit alpha (Fragment) OS=Homo sapiens GN=NACA PE=1 SV=1
0.25	78 kDa glucose-regulated protein OS=Homo sapiens GN=HSPA5 PE=1 SV=2

T3 emPAI	Target ID Aptamer T3
4.45	Keratin, type II cytoskeletal 1 OS=Homo sapiens GN=KRT1 PE=1 SV=6
2.92	Keratin, type II cytoskeletal 2 epidermal OS=Homo sapiens GN=KRT2 PE=1 SV=2
2.7	Vimentin OS=Homo sapiens GN=VIM PE=1 SV=4
0.43	Keratin, type II cytoskeletal 5 OS=Homo sapiens GN=KRT5 PE=1 SV=3
5.32	Keratin, type I cytoskeletal 10 OS=Homo sapiens GN=KRT10 PE=1 SV=6
0.45	Keratin, type I cytoskeletal 14 OS=Homo sapiens GN=KRT14 PE=1 SV=4
1.81	T-cell receptor alpha joining 56 (Fragment) OS=Homo sapiens GN=TRAJ56 PE=4 SV=1
2.62	Actin, cytoplasmic 1 OS=Homo sapiens GN=ACTB PE=1 SV=1
2.35	Actin, cytoplasmic 2 OS=Homo sapiens GN=ACTG1 PE=1 SV=1
0.46	Actin, aortic smooth muscle OS=Homo sapiens GN=ACTA2 PE=1 SV=1
0.37	Serum albumin OS=Homo sapiens GN=ALB PE=1 SV=1
1.16	Keratin, type I cytoskeletal 9 OS=Homo sapiens GN=KRT9 PE=1 SV=3
0.69	60 kDa heat shock protein, mitochondrial OS=Homo sapiens GN=HSPD1 PE=1 SV=2
0.12	Myosin-9 OS=Homo sapiens GN=MYH9 PE=1 SV=4
0.1	Isoform 2 of Myosin-10 OS=Homo sapiens GN=MYH10
0.72	Nascent polypeptide-associated complex subunit alpha (Fragment) OS=Homo sapiens GN=NACA PE=1 SV=1
0.1	Nestin OS=Homo sapiens GN=NES PE=1 SV=2
0.71	Single-stranded DNA-binding protein, mitochondrial OS=Homo sapiens GN=SSBP1 PE=1 SV=1
0.23	40S ribosomal protein S12 OS=Homo sapiens GN=RPS12 PE=1 SV=3
0.7	Serpin H1 (Fragment) OS=Homo sapiens GN=SERPINH1 PE=1 SV=2
0.43	Transcription factor BTF3 homolog 4 OS=Homo sapiens GN=BTF3L4 PE=1 SV=1
0.29	Reticulocalbin-2 OS=Homo sapiens GN=RCN2 PE=1 SV=1
0.26	Prelamin-A/C OS=Homo sapiens GN=LMNA PE=1 SV=1
0.12	THO complex subunit 4 OS=Homo sapiens GN=ALYREF PE=1 SV=1
0.16	Nuclease-sensitive element-binding protein 1 (Fragment) OS=Homo sapiens GN=YBX1 PE=1 SV=1
0.3	Peptidyl-prolyl cis-trans isomerase B OS=Homo sapiens GN=PPIB PE=1 SV=2
0.1	Isoform 2 of Heat shock protein HSP 90-alpha OS=Homo sapiens GN=HSP90AA1
0.12	Heat shock protein HSP 90-beta OS=Homo sapiens GN=HSP90AB1 PE=1 SV=4

Supplementary Figure 1: Hyperphosphorylative conditions. SH SY5Y cells differentiated with 30µM Retinoic acid for 10days were exposed to 30nM Okadaic acid for 24hrs. Under these hyperphosphorylative conditions tau is overexpressed and hyperphosphorylated. Figure shows the presence of ptau Ser202/Thr205 stained with antibody AT8 and p-tau 396 in SH SY5Y cells in hyperphosphorylative conditions..

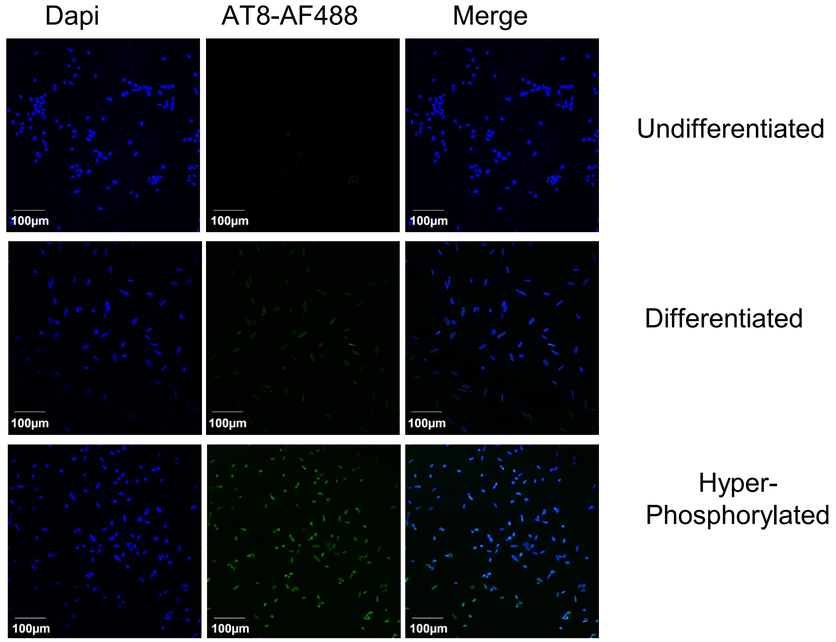

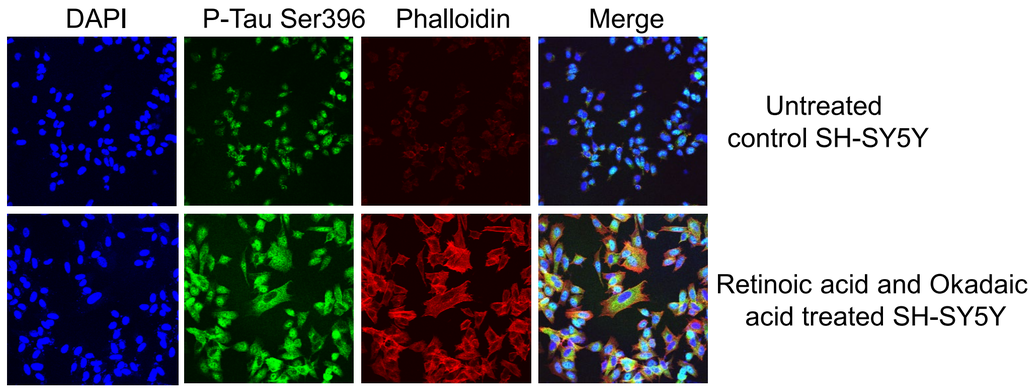
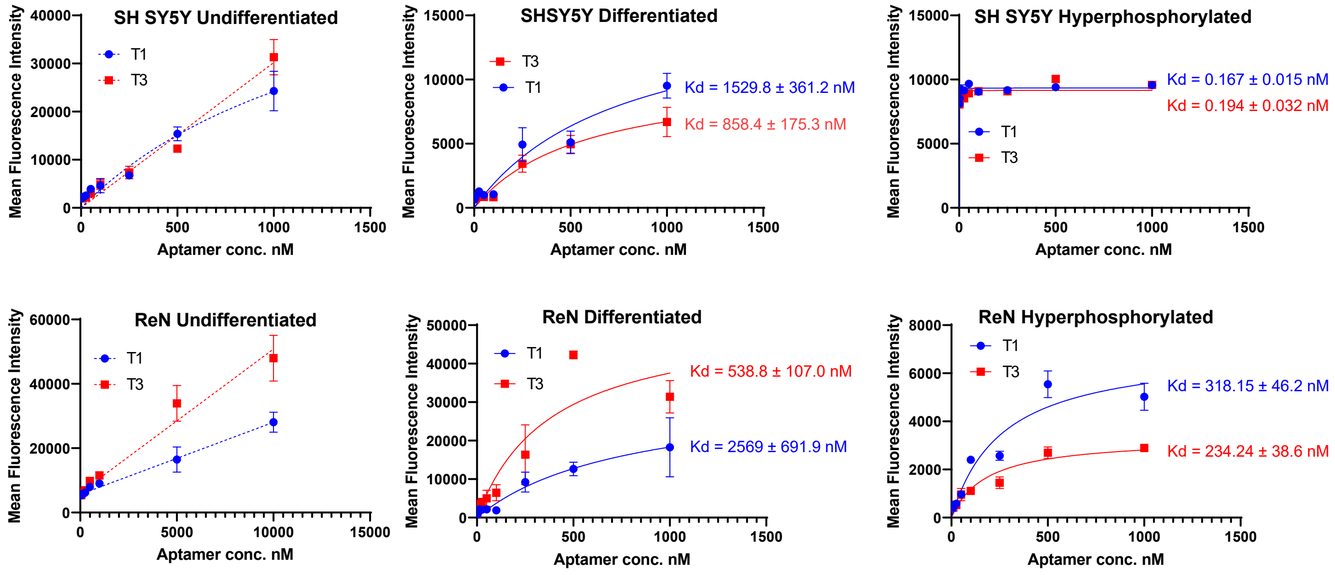
Supplementary Figure 2: Apparent dissociation constants of Aptamer T1 and T3Target. SH SY5Y and Ren cells were grown in 96-well plates, Retinoic acid was used for differentiation. Okadaic acid for SH SY5Y and quinolinic acid for ReN cells was used to generate hyperphosphorylative conditions. Saturation binding curves were generated using Cy5 labelled T1 and T3 using a microplate fluorescent reader. The binding constant Kd apparent was calculated using the inbuilt modules in Graph Pad Prism. * *error bars smaller than symbol not visualized* *NAME THE MODULE*